Processing and surface modification of titanium open cell porous structures for PEM fuel cell bipolar plates

Carlos Romero [a,b,1,*], Davide Benedetto [a], Elena Gordo [a,b]

[a] Department of Materials Science and Engineering, Universidad Carlos III de Madrid, Leganés 28911 Spain
[b] Instituto Álvaro Alonso Barba (IAAB), Universidad Carlos III de Madrid, Leganés 28911 Spain

HIGHLIGHTS

- Powder metallurgy is feasible for alternative PEM fuel cell bipolar plate designs.
- Open cell porous Ti with a variety of features meets the target properties.
- Gas nitriding is an effective way to improve ICR and corrosion performance of Ti.

ARTICLE INFO

ABSTRACT

Bipolar plate (BP) and porous transport layer (PTL) materials and designs are critical for the performance of a proton exchange membrane fuel cell (PEMFC) and electrolyser (PEMEC) due to their role as fluid distributor and electron transporter between cells. Designs based on open cell porous structures require a good control on the porosity features. The aim of this work is to use powder metallurgy to manufacture titanium porous structures and the use of suitable surface modification techniques that can improve the performance of the PEM systems, focusing on fuel cells. Using the space holder method, porous structures of up to 63% porosity and controlled pore size can be processed to tailor the characteristics for an optimal design and, through a simple gas nitriding treatment, the performance of the material in terms of interfacial contact resistance (below 10 mΩcm^2 after corrosion) and corrosion resistance (below 1 μAcm^{-2}) are improved for both dense and porous structures.
© 2023 The Author(s). Published by Elsevier Ltd on behalf of Hydrogen Energy Publications LLC. This is an open access article under the CC BY license (http://creativecommons.org/licenses/by/4.0/).

Introduction

Bipolar plates (BP) and porous transport layers (PTL) in proton-exchange membrane fuel cells (PEMFC) and water electrolysers (PEMWE) are stack components that, even though they do not take direct part in the electrochemical reactions, are key to the performance of the cells because they are responsible for the distribution of gases, transfer of electrons between cells, heat management and the mechanical integrity of the cell [1]. A bad design or choice of materials and processes can result in a poor performance of the system.

Metallic BPs (in PEMFC and PEMWE) and PTLs (in PEMWE) are the materials of choice because of their higher mechanical

---

strength, that is able to sustain forming operations and assembly loads, and their cheaper manufacturing in mass-scale, compared to graphite and polymer composites [2]. They have two main issues. The first one is corrosion, that could result in poisoning of the membrane from the dissolved ions [3]. The second issue is the electrical interfacial contact resistance (ICR) between the components, because a drop of potential happens, and it is a common issue of corrosion resistant metals and alloys, because they develop passivated layers that are essentially insulating. Both these issues can be solved with surface treatments that protect the substrate and increase the electrical conductivity of the surface [4].

Coated stainless steels are highly sought after because of their low cost, high formability, and controlled corrosion rates for these applications [2]. However, titanium remains still as a strong candidate for BP and PTL because of its excellent corrosion resistance even with an untreated surface, but the high cost of the raw material and its lower formability are its main drawbacks [5]. Commercially pure Ti (like grade 2) can only be formed to a limited degree before they fracture, reaching maximum channel depths of around 0.3 μm for sheets of 0.1 μm thickness, therefore one important area of work is that of the prediction of failure during forming [6] and the design of the tooling and forming processes [7]. Additionally, welding these plates can cause deformation due to their low thickness [8], and there are no systematic studies on welding titanium plates apart from some reported data [9]. Despite these challenges being key to the mass-production of titanium BPs, the main focus on the research and development of these components is that of the coatings.

The most standard materials used in coating of Ti BPs are precious metals like gold or platinum, but due to their high cost − that hinders mass-use- other alternative compounds are being researched, like carbon, metal nitrides, carbides or even conducting polymers [10]. For instance, titanium carbide [11] or composite coatings made of conductive polymers reinforced with conductive nanoparticles, like PTFE-TiN [12], display good corrosion protection and are conductive enough to present low ICR as well. Of the coating materials used, TiN is the most interesting to overcome the problem of passivation and contribute to an improved corrosion resistance [13]. Typical TiN coatings are obtained using physical methods like magnetron sputtering [13], multi-arc ion plating [14] or HiPIMS [15], which result in thin and compact coatings and can be incorporated to substrates of different metals. For Ti substrates, thermochemical treatments like gas nitriding [16], also with the assistance of plasma or laser [17], or electrochemical nitriding [18] are an option because there is already Ti on the surface and only N has to be incorporated. Gas (or thermal) nitriding has potential advantages in terms of simplicity of the process and that it can be used to coat surfaces without requirements on the geometry and requires minimal equipment but it requires higher temperatures [19].

New designs for the BP in PEMFC and the BP + PTL in PEMWE are showing that removing the channels of the BP and substituting them by a porous structure can match and even improve the performance of the cell, while considerably simplifying the manufacturing process and reducing costs [20−23]. In the case of BPs in PEMFC, these designs improve the mass transport, reduce pressure drops and increases the

mixing compared to a conventional channelled structure [22]. However, the work in the porous flow fields for BPs of PEMFCs have been limited to foams with large porosities and large pore size, and the optimized features have yet to be obtained.

The progress in better designs of BP and BP + PTL based on porous structures lies in being able to obtain porous structures with a variety of features like pore size distribution and porosity, and to obtain layered or gradient structures for advanced designs. A technology that can implement this for a variety of metals and alloys is powder metallurgy (PM) by sintering loose or lightly pressed powders (more restricted in terms of pore size and volume) [24] or using the space-holder method (very flexible route for pore size and porosity) [25], with the advantage that is a technology that can be adapted for mass production of porous parts. This technology can be used for Ti and steel, among other alloys, and in the case of titanium it is also the only and most cost-effective way to produce these structures. Additionally, the main technologies to coat conventional BPs are not suitable for these porous designs, at least considering if they can coat the complete structure. For these, techniques that do not rely on line-of-sight have to be used, like wet-chemical approaches or CVD. In the case of TiN coatings, gas nitriding has the potential to be a very useful technology.

In this work, the feasibility of powder metallurgy to manufacture materials for PEMFC BP based on porous structures is explored, focusing on Ti as it proves the most potential to improve the conventional Ti BP. Surface modification using gas nitriding is performed to obtain TiN on the surface, and an alternative approach is designed to reduce the cost of the nitriding process, taking advantage of the fact that sintering is performed at similar temperatures than the nitriding. The performance of these materials is also studied, using the targets set by the US Department of Energy [26] for PEMFC BP as reference.

Materials and experimental procedure

Processing of substrates and surface modification

The dense and porous titanium specimens were processed via PM routes, complemented with the space holder technique for the porous materials. The Ti samples were processed using TiH$_2$ (GfE Metalle und Materialien GmbH) with a maximum particle size of 63 μm as the Ti precursor. The chemical composition of the TiH2 powder is shown in Table 1. For the fabrication of porous specimens, ammonium bicarbonate (NH$_4$HCO$_3$, Sigma Adrich BioUltra, purity ≥99.5%) was used as a space holder.

Dense samples were prepared by directly using the TiH$_2$ powders, pressed uniaxially into disks of 16 mm of diameter and 2−3 mm of height, using a compaction pressure of 200 MPa. In the case of porous samples with targeted porosity, these were prepared by mixing the TiH$_2$ powder with sieved NH$_4$HCO$_3$ particles, under different volume ratios to target different porosities. Mixing was performed during 1 h at 50 rpm and the mixtures were pressed uniaxially at 200 MPa. The space holder was removed by placing the samples in a muffle at 50 °C for 6 h. Then, both dense and porous samples were sintered in a

Table 1 – Chemical composition of TiH$_2$ powder.

Fe (wt.%)	C (wt.%)	N (wt.%)	O (wt.%)	H (wt.%)	Ti (wt.%)
≤0.070	≤0.050	≤0.050	≤0.45	≥3.0	Balance

high vacuum furnace at 1250 °C for 2 h, using a heating curve of 5 °C/min until 450 °C, 2 °C/min between 450 and 650 °C and 5 °C/min between 650 °C and the sintering temperature, plus cooling at 5 °C/min until room temperature. These conditions were optimized previously to ensure decomposition of TiH$_2$ into Ti. Additionally, an alternative sintering atmosphere was also tried, using 1 bar Ar of purity 2X, at 1000 and 1200 °C with similar heating and cooling rates.

Surface modification was performed on the dense substrates using gas nitriding to develop a dense layer of TiN on the surface of the substrates. The samples were heated at 5 °C/min in a furnace under 1 bar N$_2$ atmosphere until the target temperature of 950 or 1000 °C, and the temperature was held for 2 h.

An alternative route to obtaining the nitrided structures was to combine the sintering and nitriding in the same furnace run. For this, the higher temperature of 1000 °C was chosen to ensure the sinterability. The samples were placed in a ceramic tube and heated up to 1000 °C using the similar heating curves as for conventional sintering, the temperature was then held for 3 h and then cooled to room temperature at 5 °C/min. The initial atmosphere was 1 bar Ar, held until 1 h at 1000 °C and then the atmosphere was switched to N$_2$. A diagram depicting the two type of sintering and nitriding cycles is shown in Fig. 1.

Microstructural analysis and density

The density of the samples was characterized using the Archimedes' method in acetone at room temperature, measuring the dry, saturated and immersed weights. To ensure total filling of the pores with the solvent, the samples immersed were previously degassed. The porosity was calculated following Eq. (1), where ρ_{Arch} is the measured density and ρ_{bulk} is the bulk density of c. p. Ti, 4.51 g/cm^3.

$$Porosity\ (\%) = 100*\left(1 - \frac{\rho_{Arch}}{\rho_{bulk}}\right) \quad (1)$$

Optical microscopy was performed on metallographically prepared specimens to study the features of the porosity, using ImageJ [27] to process the images. To obtain a continuous pore size distribution of the images, the xlib plug-in was used, based on [28].

Scanning electron microscopy (SEM) a FEI Teneo, equipped with a microanalysis probe was also used to study the morphology of the surfaces.

X-ray diffraction

For untreated titanium specimens, conventional x-ray diffraction (XRD) was used in a X'Pert MPD diffractometer, with a Bragg-Brentano configuration and a Cu anode as x-ray source. The range studied was between 30° and 80°, step size of 0.02° and 1 s per step. Grazing angle X-ray diffraction (GA-XRD) using

an incident angle of 1.5° was performed on the nitrided specimens, in an X'pert MRD diffractometer with a Bragg-Brentano configuration, using a Cu anode, in a range between 30° and 80° with a step size of 0.02° and 3 s per step. The incident angle results in a penetration of the x-rays of around 0.75 μm.

X-ray photoelectron spectroscopy

X-ray photoelectron spectroscopy (XPS) was used to measure the composition and the chemical state of the surfaces of the untreated and nitrided titanium. An Al x-ray source was used in a Fisons Instrument VG Microtech MT-500 spectrometer on as-received surfaces.

Three-point bending

Three-point bending tests were performed on dense and porous rectangular specimens with dimensions of roughly 4 × 11 × 28 mm (thickness, width and length), with a distance of 23 mm between the contact points and a load cell of 15 kN and coupled with an extensometer. Before testing samples were ground up to grit size 1000 using SiC paper.

Corrosion

Corrosion tests were performed using a three-electrode cell, with a platinized-Ti counter electrode and a Ag/AgCl reference electrode in a solution of H$_2$SO$_4$ with pH = 3 at 70 °C. For the anodic conditions, the test consisted on a polarization curve between −0.4 and 0.6 V vs Ag/AgCl under Ar purge, while the cathodic conditions were evaluated using chronoamperometry for 24 h at 0.6 V vs Ag/AgCl with air bubbling.

Interfacial contact resistance

Interfacial contact resistance (ICR) was measured using carbon gas diffusion layer (SIGRACET GDL 28 BCE), a DC power supply using 2 A of current, Au-coated copper plates and a micromechanical testing machine (Microtest, Spain) that can apply up to 5 kN of load. Measurements were done according to Wang's method [29], performed by measuring first the voltage drop of a wafer of GDL with the same contact area as the sample for different loads (V1), and then measuring the voltage drop of the sample sandwiched in between the GDLs (V2). The ICR is calculated following Eq. (2), where I is the current and A is the cross-sectional area of the specimen:

$$ICR = \frac{V_2 - V_1}{I}\frac{A}{2} \quad (2)$$

Pristine specimens with surface modification were tested as-obtained while untreated samples were tested after grinding using SiC paper up to 2000 grit size. ICR was also measured on specimens after corrosion testing.
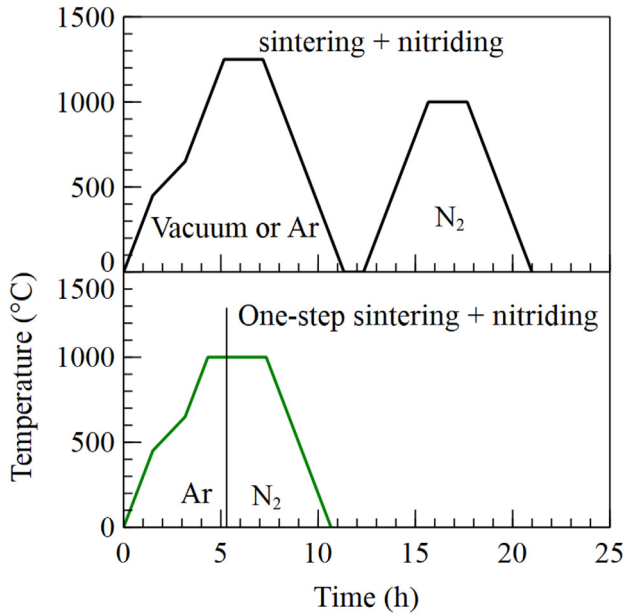
Fig. 1 — Sintering and nitriding curves.

Results and discussion

Characterization of the substrates

Fig. 2 shows the microstructures of the porous Ti structures obtained through the space holder method with different targeted porosities and pore sizes. The porosity is mostly interconnected, with a low degree of isolated pores. The structure is more connected and homogeneous when moving towards higher targeted porosities and smaller pore sizes, as can be seen comparing Fig. 2a and b. The structures are homogeneous and do not show fractures or collapses associated to the removal of the space holder, which means that the mixing parameters, volume ratios and particle sizes are appropriate for manufacturing these porous structures.

The densities of the Ti structures are shown in Fig. 2c. The obtained porosities are lower than the targeted values (the SH vol%) when using the Archimedes' test, which is a reliable 3D characterization technique. This would be related to the contraction experienced during the dehydrogenation of TiH_2 during sintering, as that transformation has a shrinkage of around 20%. Additionally, for the same space holder volume, the total porosity does not change with different particle sizes, so it mostly depends on the space holder volume. IA reveals
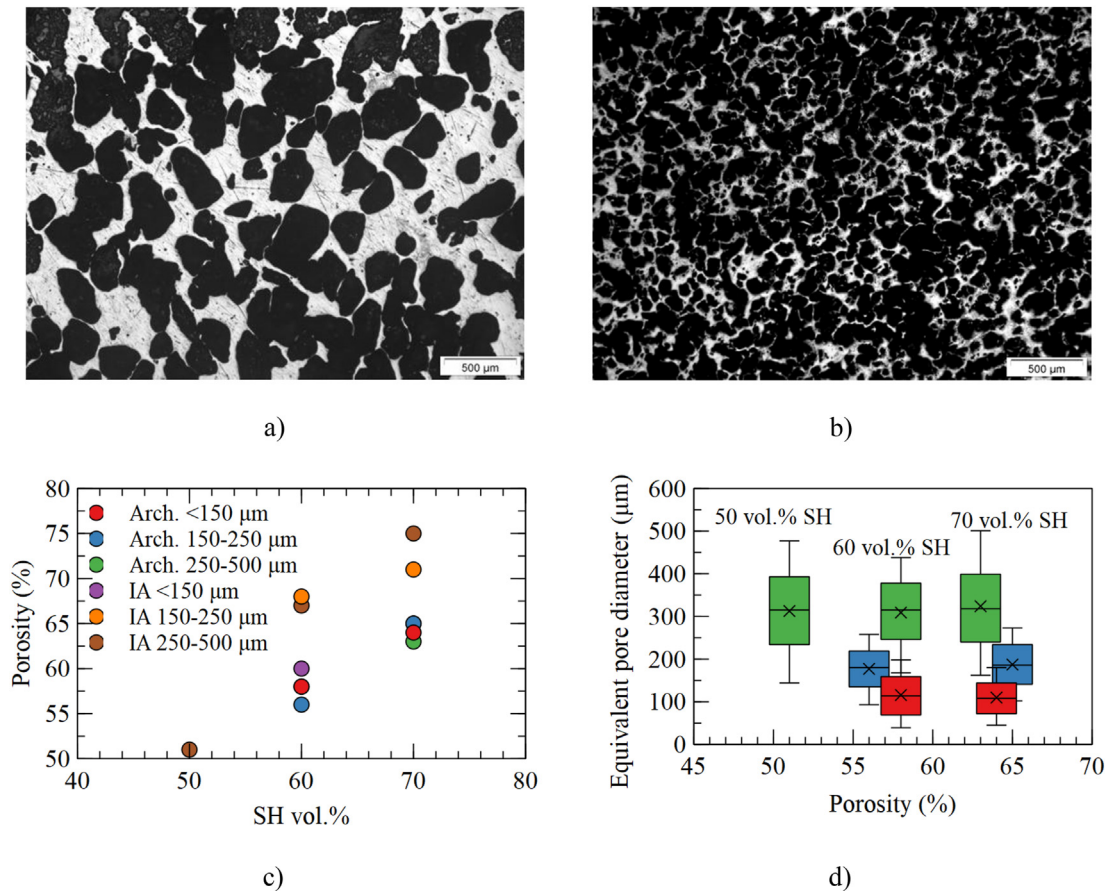

Fig. 2 — Porosity analysis of porous Ti with different volume and size of space holder (SH): a) 60 vol% and 250—500 μm, b) 70 vol% and <150 μm, c) total porosity and d) pore size distribution in terms of SH volume and size.

pore sizes that, after the 2D to 3D correction of metallographical features (multiplying by a factor of 1.5x), are centered within the range of the targeted space holder size (Fig. 2d). The pore size distribution obtained with the method reveals a good control, and clear differences between the ranges studied. Using the spheres method, the targeted pore size lies between the d25 and d90 of the distribution, covering 65% of the total pore volume. Only 10% of the pore volume is above the targeted range, while 25% are below. However, the irregular and angular morphology of the SH is very far from that of a sphere, so the model requires very small spheres to accommodate the irregularities, which explains the larger value below the target. These results reveal that the space holder technique can produce titanium foams with an excellent control of the porosity features.

The mechanical properties of these structures, measured using three-point bending tests, are shown in Fig. 3. There is a clear relationship between the transverse rupture strength (TRS) and the total porosity of the porous structures, with a sharp decay once the porosity is increased using the space holder method (Fig. 3a). It must be noted that the effect of the pore size does not affect the TRS significantly, so the properties are mostly defined by the total porosity of the material. For applying these materials for PEMFC BPs, the requirement in terms of mechanical properties is that the TRS is above 25 MPa [26], and all these materials satisfy the requirement with ample margin. The flexural modulus also presents a large decay for porous structures, with values around 10–15% of the bulk Young Modulus, and it is mostly independent on the pore size distribution (Fig. 3b). Fig. 3c shows stress-strain curves at the middle point. The curves have a similar shape: a quasi-linear elastic region at the beginning, followed by a short plastic region just before reaching the TRS and then the structures enter the crack propagation regime, characterized by a slow propagation of the crack and a decrease in the stress.

The fracture surface of after three-point bending test of the porous structure with 60 vol% of SH and a size distribution of 150–250 μm is shown in Fig. 3d. It can be seen that pores are homogeneously distributed and interconnected, and that cracks from space holder removal are missing, confirming what the 2D microstructures established. The fracture surfaces show that the material fails in a brittle manner, with signs of cleavage (red arrows), due to the elevated local stresses that the material undergoes, and match with the small amount of plastic deformation before crack propagation seen in the stress-strain curves. White arrows show the paths between pores that were interconnected, only a small section of the area is formed by material struts that are bearing load.

Characterization of the surface-modified substrates

The grazing incidence XRD patterns of the as-sintered Ti, nitrided Ti at two temperatures and nitrided Ti processed in one step are shown in Fig. 4. The as-sintered Ti presents a composition of purely α phase, without traces of TiH_x, showing that the decomposition of the initial TiH_x into Ti was completed, consistent with previous results in the literature, that indicated that a slower heating rate in the range of hydride decomposition ensured the loss of most H [30]. The nitrided specimens all show thin films composed of TiN and

Ti_2N in different proportions. For the dedicated nitriding treatment of sintered Ti, a larger amount of TiN is obtained within the 0.75 μm analysed after treatment at 1000 °C compared to 950 °C, which has roughly similar amounts of TiN and Ti_2N. Due to the gradient in composition typical of this treatment, the compound richer in N, TiN, is formed on the outer surface of the film, while the leaner compound, Ti_2N, is formed in the interior of the film. Both phases are equally stable at the nitriding temperatures of 950 and 1000 °C, and the larger amount of TiN in the specimens nitrided at 1000 °C is associated to a thicker external layer, by an increase in the diffusion rate. In the case of the one-step sintering + nitriding, the main phase Ti_2N and the minority phase is TiN. The material was nitrided at the same temperature (1000 °C) and time (2 h) that the pre-sintered counterpart, so the lower amount of TiN, associated to a thinner layer of the compound, can be related to a shorter exposure to a fully N_2 atmosphere. This is because, once the input gas is switched to N_2 from Ar, there is a transient regime where the N content of the atmosphere increases from 0 to 100%. The processing conditions for the one-step sintering + nitriding can be, therefore, optimized, to achieve similar composition than the dedicated nitriding of sintered or consolidated Ti.

The Ti 2p XPS fitted spectra of the surfaces of untreated and treated Ti are shown in Fig. 5. Four oxidation states were considered according to the literature: 0,+2, +3 and + 4 [31]. The as-sintered Ti (Fig. 5a) has a surface where Ti is in a chemical state of 4+, which is associated with the native TiO_2 film. XPS has a penetration depth that usually ranges between 6 and 10 nm, indicating that the passive film is rather thick. All the nitrided surfaces show a combination of several chemical states: 0, which is associated with metallic bonds typical of TiN; 2+ and 3+, which mean that there is some degree of oxidation, associated with the presence of titanium oxynitrides $Ti_xO_yN_z$; and 4+, associated with the presence of TiO_2. Therefore, the nitrided surfaces display a combination of different phases associated to different chemical states.

The chemical states of Ti 2p were quantified and the results are shown in Table 2. Nitriding at a lower temperature resulted in a lower amount of TiN and TiO_2, and a larger amount of $Ti_xO_yN_z$, compared to nitriding at 1000 °C. Comparing the nitriding of sintered Ti with the one-step sintering + nitriding, the amount of $Ti_xO_yN_z$ remain very similar but the amount of TiN is larger for the full nitriding treatment. This is promising because the composition of the surface is not affected, therefore the performance is going to be similar, but the cost of the treatment is considerably reduced.

Structure of the thin films

Due to the nature of the film formation, which happens through diffusion of N from the surface to the bulk, the amount of N follows a gradient curve. The nitrided film is composed of two phases, which form two different layers at the micrometer level, even though they cannot be resolved at the SEM. The outer layer, richer in N, consists of TiN while the inner layer consists of Ti_2N [19]. The surface of the film, however, is not composed purely of TiN, but it is a mixture of TiN, TiO_2 and $Ti_xO_yN_z$. This is a typical feature of nitrided Ti surfaces [32]. As after the nitriding treatment the specimens are exposed to the
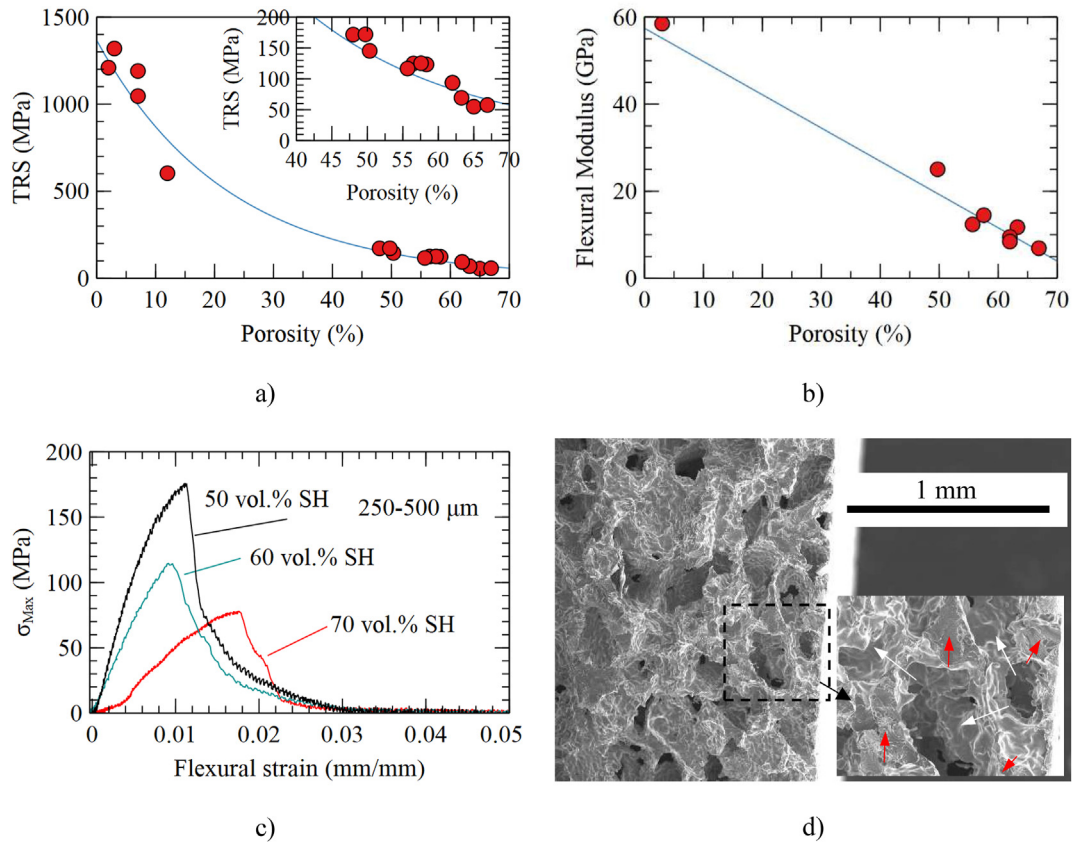
Fig. 3 – Three point bending behaviour of porous Ti structures: a) relationship between transverse rupture strength (TRS) and total porosity, b) between flexural modulus and total porosity, c) maximum stress vs flexural strain curves of structures with variable porosity, and d) fracture surface of structure with 60 vol% SH and size range of 150–250 μm.
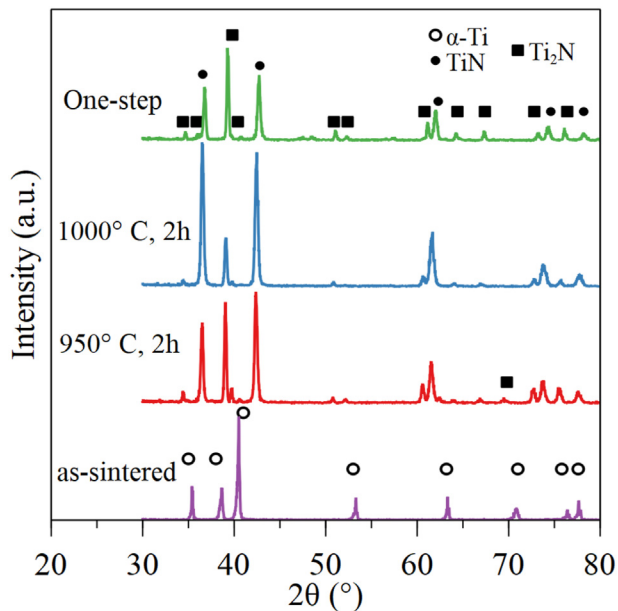
Fig. 4 – XRD patterns of as-sintered Ti and nitrided Ti at different conditions.

atmosphere, it is expected that some oxidation of the surface takes place. This process would take place again starting from the surface, therefore it can be argued that the structure of the surface resolved by the XPS is also layered. The bulk at this level is TiN, the outer surface would be TiO_2, and the intermediate layer would be composed of an oxidized $Ti_xO_yN_z$. Using DFT, Piscanec et al. discussed that minimal absorptions of O on a theoretically pure TiN surface result in the instantaneous formation of a titanium oxynitride film, with the titanium oxide layer being formed more slowly [32]. From these observations, the oxynitride is such a stable phase that is not expected to grow once it is formed, so further oxidation would be expected to happen by growth of the TiO_2 layer. A drawing showing the micro- and the nano-scale of the structures formed during the gas nitriding is shown in Fig. 6.

The oxide layer is formed because TiO_2 is more stable than TiN, in a similar way to the native layer formed on pure Ti. In this case, because TiN is more resistant to oxidation than Ti (it requires the formation of more complex compounds), the passivated TiO_2 layer is much finer on nitrided specimens compared to untreated Ti, which would be advantageous as it adds an extra protection and is thin enough to have smaller ohmic losses.
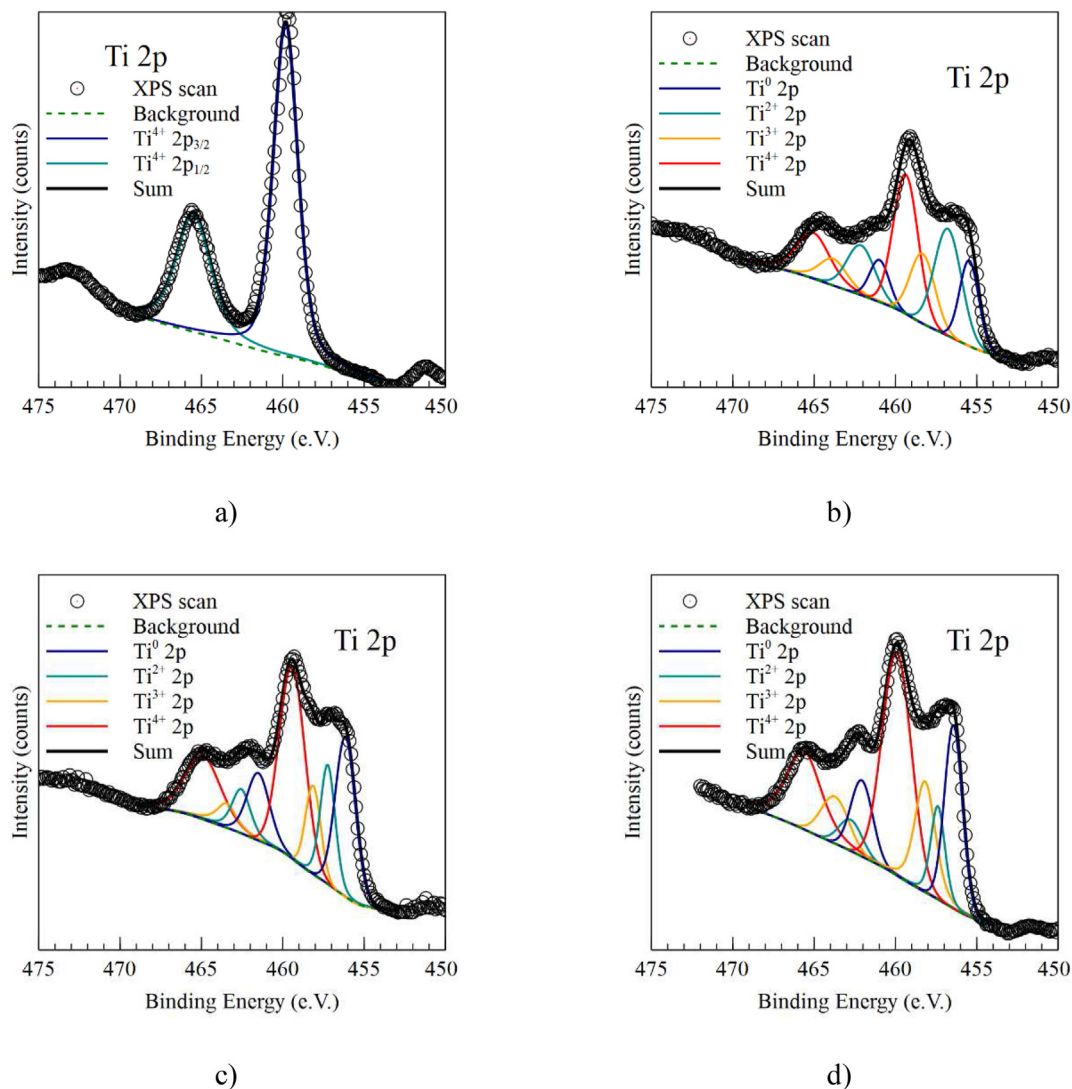
Fig. 5 — XPS spectra of Ti 2p for: a) untreated Ti, b) Ti nitrided at 950 °C, 2 h, c) Ti nitrided at 1000 °C, 2 h and d) Ti sintered and nitrided in one step at 1000 °C.

Corrosion behaviour

The corrosion behaviour of Ti, with and without the treatment, is shown in Fig. 7 for the anode and the cathode PEMFC conditions. In the case of the anode (Fig. 7a), all the conditions result in low values of corrosion current density (below 5 μAcm^{-2} at +0.6 V vs Ag/AgCl) and do not present active peaks, remaining passive in the whole range. The Ti nitrided at 950 °C displays a sudden increase on the current density

observed at different potentials which could be related to the presence of pitting corrosion or bubble formation, but the corrosion rates after the surge are still the lowest. The surface treatments of the dense Ti result in an improvement of the corrosion resistance of around 5x at the highest potential studied, +0.6 V vs Ag/AgCl, as well as in an improvement of the open circuit potential (OCP) and a reduction of the current density around the OCP. The untreated surface almost fulfils the requirements for the anode side [26], as the

Table 2 — Distribution of chemical states of Ti 2p in untreated and treated Ti.

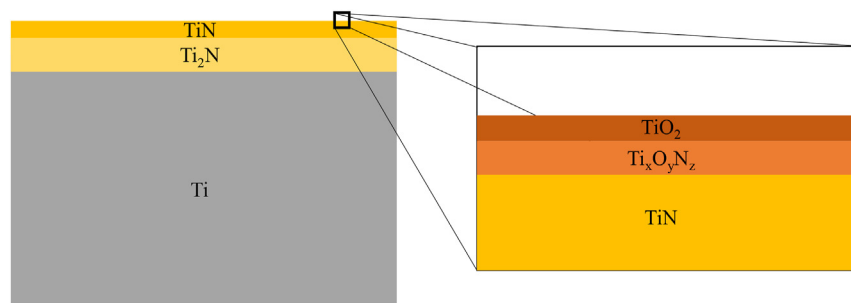|	Ti^0 (at. %)	Ti^{+2} (at. %)	Ti^{+3} (at. %)	Ti^{+4} (at. %)
As-sintered Ti	0	0	0	100
Nitrided 950 °C, 2 h	16.8	29.7	17.7	35.8
Nitrided 1000 °C, 2 h	28.7	16.8	11.7	42.8
One-step 1000 °C	23.9	18.7	10.5	46.9

Fig. 6 — Schematic drawing of the multiscale structure of the thin films grown by gas nitriding.

corrosion rate is close to the target and there are no active peaks. In the case of the nitrided Ti, both conditions satisfy the requirements of current densities below 1 μAcm^{-2}. The Tafel extrapolation of the curves (Table 3) show quantitatively that the corrosion potential after nitriding shifts towards higher values and the corrosion current densities are reduced as well, even though they remain in a similar order of magnitude.

It is important to note that the surface used for the calculation of the current density is the geometrical surface of the disks used, not the real surface. This means that, if the mechanisms of corrosion are the same, the porous specimens should have a much larger corrosion rate because of the higher exposed surface. However, the corrosion current densities are in the same order of magnitude and of very similar values. This points towards bubble formation due to the high testing temperature (70 °C in ambient pressure) in the inside of the porous structure as a probable reason that blocks the wetting of the complete structure. Comparing the porous specimens, in the anode condition, the corrosion rate of the nitrided condition is higher than that of the untreated Ti, which could be associated to the level of wetting rather than the effective corrosion rate, as the surface of the one-step treatment has similar features than the dedicated nitriding treatment.

In the case of the cathode side, which is the most critical due to the presence of O$_2$, all the materials display low corrosion current density values, with the untreated surfaces of the dense and the porous structure having stationary values after 24 h at 0.6 V vs Ag/AgCl between 1 and 2 μAcm^{-2}, which is very close to the target of the DOE of 1 μAcm^{-2} [26]. The nitrided Ti display corrosion rates that are almost one order of magnitude lower than the untreated Ti, fulfilling the requirements. Ti nitrided at 950 °C displays again the lowest current density, which is one order of magnitude lower than the other treatments and two orders of magnitude lower than that of untreated Ti.

The small difference in open circuit potential between the untreated and the treated surfaces indicate that there is not going to be a large galvanic coupling between the TiN and the substrate if defects happened on the surface, which is an important issue on TiN-coated stainless steel [33]. Therefore it is a surface modification that will ensure a high corrosion resistance in the long term, as even the substrate has low current density values, almost meeting the targets.

The XPS spectra after corrosion testing of untreated and treated Ti are shown in Fig. 8. In both cases, the chemical states present are similar to those seen in Fig. 5: for the as-sintered Ti (Fig. 8a) the surface is composed of only Ti^{4+}, associated with 100% of TiO$_2$, while the nitrided Ti (Fig. 8b) presents, after corrosion, Ti^0, Ti^{2+}, Ti^{3+} and Ti^{4+} components. The TiO$_2$ layer is still present in the untreated Ti, and it is expected to have grown due to the mechanisms of Ti corrosion, which tends to increase the thickness of the oxide layer. In the case of the nitrided Ti after corrosion, the main component is that of the external layer of TiO$_2$, but the components associated to TiN and TiON are still present, indicating that the corrosion has not resulted in an excessive growth of the oxide layer from oxidation of the nitrides.

Table 4 shows the quantification of the chemical states after deconvolution of the XPS spectra of the corroded specimens. As-sintered Ti presents 100% of TiO$_2$ associated to the passivated layer, which is similar to the structure before corrosion. The nitrided specimen has a larger amount of TiO$_2$ compared to the composition of the surface before corrosion, which grew at the expense of the titanium oxynitrides. The amount of TiN remained similar, therefore the corrosion during 24 h did not affect the inner layer considerably.

The mechanism of corrosion of Ti is associated to the presence of a very stable passive TiO$_2$ film. Under most environments, Ti behaves passively, which involves the oxidation of Ti mostly through the growth of TiO$_2$ and, in a small contribution, through its dissolution [34]. The growth of TiO$_2$ could be by two mechanisms: the growth of the native passive layer, which is dense and helps to protect against corrosion, or the growth of an outer layer on top of the passive layer, which is porous and does not protect against corrosion [34]. The untreated porous Ti shows a peak in the current density at around 12 h of testing, which could be associated to faster corrosion kinetics leading to the formation of a thicker passive layer that then is thick enough to reduce the corrosion rate, and further corrosion would happen by dissolution or growth of the porous outer layer.

In the case of nitrided Ti, the corrosion mechanism follows the reaction (3), which has a potential of −0.27 V vs RHE (Reference Hydrogen Electrode) [35].
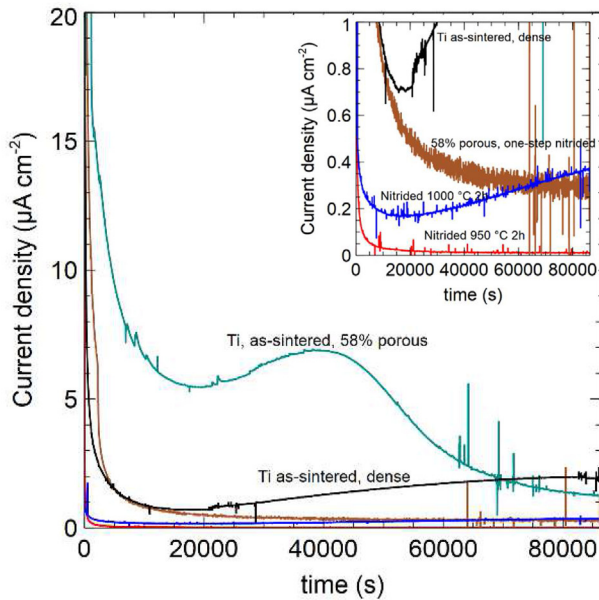
$$TiN + 2 H_2O \leftrightarrow TiO_2 + \tfrac{1}{2} N_2(g) + 4 H^+ + 4 e^- \qquad (3)$$
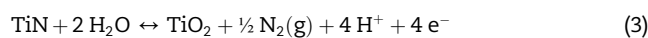
However, attending to the XPS evidence, where TiO2 and TiON are involved in the corrosion, this mechanism happens
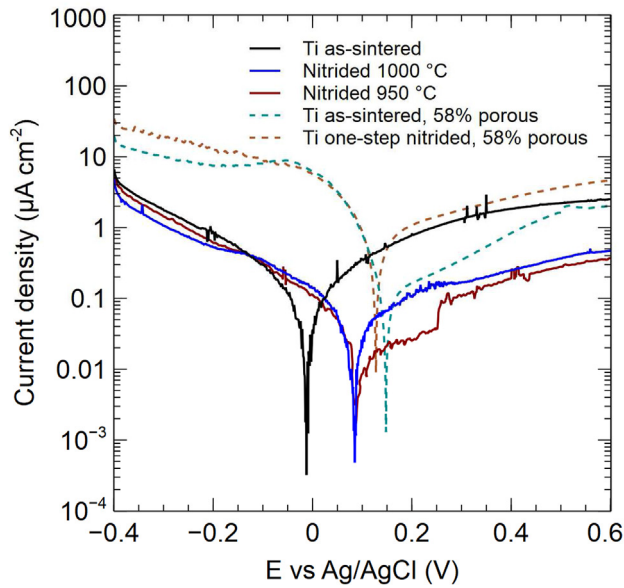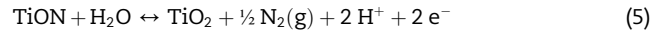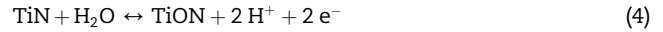
a)

b)

Fig. 7 – Corrosion tests of dense and porous Ti with and without nitriding in pH = 3 at 70 °C: a) anode side condition (Ar purge) and b) cathode side conditions (air bubbling).

by two different steps, the oxidation of TiN to form TiON (4) and the oxidation of the later into TiO_2 (5). Considering that, for the 24 h of corrosion studied, the layer of TiN was not affected and the corrosion happened by growth of TiO2 from oxidation of TiON, the kinetics of reaction (5) must be much faster than those of reaction (4).

$$TiN + H_2O \leftrightarrow TiON + 2\,H^+ + 2\,e^- \tag{4}$$

$$TiON + H_2O \leftrightarrow TiO_2 + \tfrac{1}{2}\,N_2(g) + 2\,H^+ + 2\,e^- \tag{5}$$

This is assuming that these mechanisms are more prone to happen than the dissolution of Ti^{4+}, as discussed in Ref. [35] These reactions require the diffusion through the titanium oxide and oxynitride layers, which slows down the corrosion rates, as seen in the tests when comparing the untreated with the nitrided Ti.

Interfacial contact resistance

The interfacial contact resistance (ICR) curves of the untreated and treated Ti, in the dense and porous configuration, are shown in Fig. 9a. The untreated Ti surfaces present a very high ICR, associated to the passive TiO_2 layer. The formation of a TiN layer on the surface after a nitriding treatment is able to improve the ICR of both alloys to below 10 Ωcm^2, which is the US DOE target for materials used in BP [26].

After corrosion for 24 h at 0.6 V vs Ag/AgCl, the ICR of all the conditions increased (Fig. 9b), which is expected due to the passivation of the surface. The ICR of dense, untreated Ti increased from 442 to 480 $m\Omega cm^2$ (increase of 8%), dense and that of porous untreated Ti increased from 91 to 153 $m\Omega cm^2$ (increase of 68%). In the case of dense nitrided Ti, the ICR increased from 8 to 11 and for the porous nitrided Ti, from 5 to 7 $m\Omega cm^2$, both resulting in an increase of 36%. Both treated conditions fulfil the requirements even after 24 h of accelerated testing.

The effect of porosity is not detrimental to the ICR, as both porous substrates present similar or lower ICR than the dense counterparts. If the contact surface considering the porosity (instead of the nominal dimensions) was used, the ICR of the porous materials would be even lower. However, the deformation of the GDL with pressure would increase the effective contact area of the porous material, reducing the effect that porosity had. The large differences on benefit of the porous Ti could be attributed to the surface TiO_2 layer, which could have variable thickness. Treatments to remove this layer could be applied so that the different conditions begin from a similar state, but this would mean that, when the BPs are in operation, the re-passivation of the surface would be quick, reaching similar levels again to what is being shown here.

Table 3 – Tafel parameters of the polarization curves for anode side testing.						
		E_{corr} (V)	$i_{0,an}$ (μAcm^{-2})	β_{an} (mV/decade)	$i_{0,cat}$ (μAcm^{-2})	β_{cat} (mV/decade)
Dense	Ti as-sintered	−0.02	0.098	210	0.094	184
	Nitrided 950 °C	0.06	0.010	369	0.026	220
	Nitrided 1000 °C	0.09	0.042	277	0.062	239
Porous (58%)	Ti as-sintered	0.15	0.096	262	0.127	55
	One-step nitrided	0.13	0.674	327	0.695	98

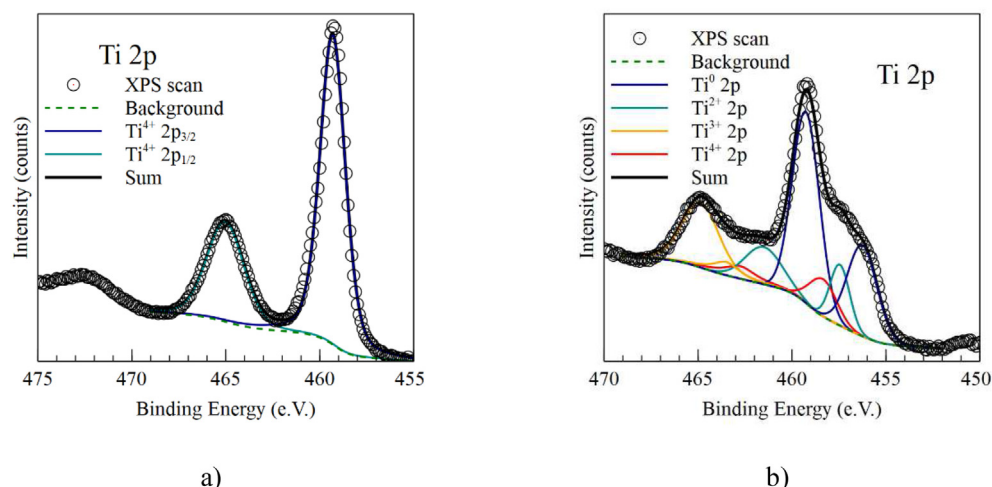a)   b)

Fig. 8 – Ti 2p XPS spectra of Ti after potentiostatic testing at 0.6 V vs Ag/AgCl: a) as-sintered and b) nitrided at 950 °C.

Table 4 – Distribution of chemical states of Ti 2p after corrosion testing of as-sintered and nitrided Ti.

	Ti^0 (at. %)	Ti^{+2} (at. %)	Ti^{+3} (at. %)	Ti^{+4} (at. %)
As-sintered Ti	0	0	0	100
Nitrided 950 °C, 2 h	27.1	11.7	10.0	51.1

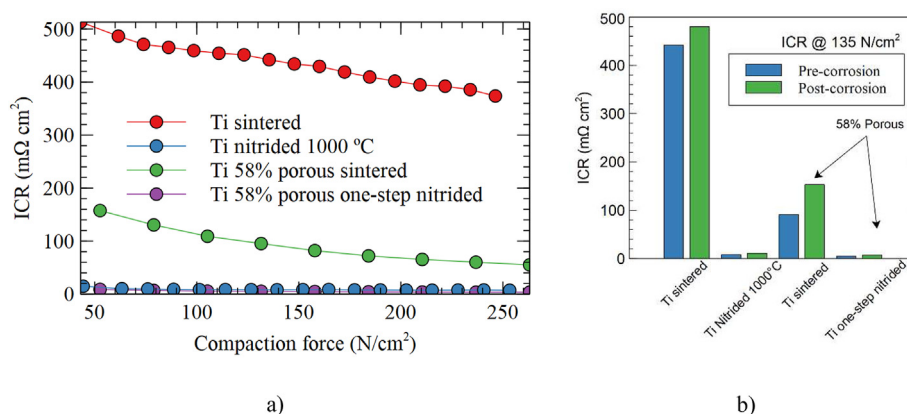a)   b)

Fig. 9 – Interfacial contact resistance (ICR) of untreated and treated titanium: a) evolution with compaction force in pristine state, b) comparison of pre- and post-corrosion measured at 135 N/cm^2.

Conclusions

The aim of this work was to develop powder metallurgy and post-processing approaches for manufacturing cost-effective titanium bipolar plates for PEMFC, especially taking into consideration its potential for the development of alternative flow field designs through porous structures.

- Open cell porous Ti structures can be produced with defined pore size distributions and porosity levels using the space holder technique. These structures have total interconnection between pores and they have sufficient flexural strength and stiffness to sustain the loads and bring structural integrity to the assembly. The transverse rupture strength of the structures decreases with an increase in the porosity, and is around 50 MPa for those with the highest porosity, which fulfil the target value of 25 MPa from the DoE.
- Surface modification through gas nitriding results in a multi-layered structure with a TiN film with thickness of several hundreds of nm. The surface of the film is composed of layers of TiO$_2$, Ti oxynitride (TiON) and TiN. Sintering and nitriding in one step results in films with similar composition, obtained in a much more cost-effective way.
- The presence of an external nm-thick TiO$_2$ layer after gas nitriding is not detrimental to the ICR, as the treated Ti

conditions have values below 10 mΩcm^2, reaching the targets for the application. In the case of the untreated conditions, the ICR at 135 N/cm^2 is of 91 and 440 mΩcm^2 for the porous and dense titanium.

- The treatments also improve the corrosion resistance in almost one order of magnitude compared to the untreated Ti and are able to keep the ICR in low values even after 24 h in corrosion conditions. While for untreated Ti, the ICR increases at least 40 mΩcm^2, a nitrided Ti experiences only an increase around 2 mΩcm^2. This is due to the stable nature of TiN and TiON, which reduce significantly the growth of the insulating TiO$_2$ layer.

Declaration of competing interest

The authors declare that they have no known competing financial interests or personal relationships that could have appeared to influence the work reported in this paper.

Acknowledgements

REFERENCES

[1] Hermann A, Chaudhuri T, Spagnol P. Bipolar plates for PEM fuel cells: a review. Int J Hydrogen Energy 2005;30:1297–302. https://doi.org/10.1016/j.ijhydene.2005.04.016.

[2] Stein T, Ein-Eli Y. Challenges and perspectives of metal-based proton exchange membrane's bipolar plates: exploring durability and longevity. Energy Technol 2020;8:1–13. https://doi.org/10.1002/ente.202000007.

[3] Mo J, Steen SM, Zhang FY, Toops TJ, Brady MP, Green JB. Electrochemical investigation of stainless steel corrosion in a proton exchange membrane electrolyzer cell. Int J Hydrogen Energy 2015;40:12506–11. https://doi.org/10.1016/j.ijhydene.2015.07.061.

[4] Asri NF, Husaini T, Sulong AB, Majlan EH, Daud WRW. Coating of stainless steel and titanium bipolar plates for anticorrosion in PEMFC: a review. Int J Hydrogen Energy 2017;42:9135–48. https://doi.org/10.1016/j.ijhydene.2016.06.241.

[5] Xu Z, Qiu D, Yi P, Peng L, Lai X. Towards mass applications: a review on the challenges and developments in metallic bipolar plates for PEMFC. Prog Nat Sci: Mater Int 2020;30:815–24. https://doi.org/10.1016/j.pnsc.2020.10.015.

[6] Modanloo V, Talebi-Ghadikolaee H, Alimirzaloo V, Elyasi M. Fracture prediction in the stamping of titanium bipolar plate for PEM fuel cells. Int J Hydrogen Energy 2021;46:5729–39. https://doi.org/10.1016/j.ijhydene.2020.11.088.

[7] Wu Z, Cao Q, Fu J, Li Z, Wan Y, Chen Q, Li L, Han X. An inner-field uniform pressure actuator with high performance and its application to titanium bipolar plate forming. Int J Mach Tool Manufact 2020;155. https://doi.org/10.1016/j.ijmachtools.2020.103570.

[8] Yi P, Du X, Kan Y, Peng L, Lai X. Modeling and experimental study of laser welding distortion of thin metallic bipolar plates for PEM fuel cells. Int J Hydrogen Energy 2015;40:4850–60. https://doi.org/10.1016/j.ijhydene.2015.02.025.

[9] Ren Z, Zhang D, Wang Z. Stacks with TiN/titanium as the bipolar plate for PEMFCs. Energy 2012;48:577–81. https://doi.org/10.1016/j.energy.2012.10.020.

[10] Teuku H, Alshami I, Goh J, Masdar MS, Loh KS. Review on bipolar plates for low-temperature polymer electrolyte membrane water electrolyzer. Int J Energy Res 2021;45:20583–600. https://doi.org/10.1002/er.7182.

[11] Shi J, Zhang P, Han Y, Wang H, Wang X, Yu Y, Sun J. Investigation on electrochemical behavior and surface conductivity of titanium carbide modified Ti bipolar plate of PEMFC. Int J Hydrogen Energy 2020;45:10050–8. https://doi.org/10.1016/j.ijhydene.2020.01.203.

[12] Gao P, Xie Z, Wu X, Ouyang C, Lei T, Yang P, Liu C, Wang J, Ouyang T, Huang Q. Development of Ti bipolar plates with carbon/PTFE/TiN composites coating for PEMFCs. Int J Hydrogen Energy 2018;43:20947–58. https://doi.org/10.1016/j.ijhydene.2018.09.046.

[13] Jannat S, Rashtchi H, Atapour M, Golozar MA, Elmkhah H, Zhiani M. Preparation and performance of nanometric Ti/TiN multi-layer physical vapor deposited coating on 316L stainless steel as bipolar plate for proton exchange membrane fuel cells. J Power Sources 2019;435:226818. https://doi.org/10.1016/j.jpowsour.2019.226818.

[14] Zhang D, Duan L, Guo L, Wang Z, Zhao J, Tuan WH, Niihara K. TiN-coated titanium as the bipolar plate for PEMFC by multi-arc ion plating. Int J Hydrogen Energy 2011;36:9155–61. https://doi.org/10.1016/j.ijhydene.2011.04.123.

[15] Elmkhah H, Attarzadeh F, Fattah-alhosseini A, Kim KH. Microstructural and electrochemical comparison between TiN coatings deposited through HIPIMS and DCMS techniques. J Alloys Compd 2018;735:422–9. https://doi.org/10.1016/j.jallcom.2017.11.162.

[16] Lee H, Kang H, Kim J, Shin HK, Lee J, Huh SH, Sung J, Lee HJ. Inward diffusion of Al and Ti3Al compound formation in the Ti-6Al-4V alloy during high temperature gas nitriding. Surf Coat Technol 2014;240:221–5. https://doi.org/10.1016/j.surfcoat.2013.12.027.

[17] Biswas A, Li L, Chatterjee UK, Manna I, Majumdar JD. Diode laser assisted surface nitriding of Ti-6Al-4V: properties of the nitrided surface. Metall Mater Trans A Phys Metall Mater Sci 2009;40:3031–7. https://doi.org/10.1007/s11661-009-0021-0.

[18] Jin J, He Z, Zhao X. Formation of a protective TiN layer by liquid phase plasma electrolytic nitridation on Ti–6Al–4V bipolar plates for PEMFC. Int J Hydrogen Energy 2020;45:12489–500. https://doi.org/10.1016/j.ijhydene.2020.02.152.

[19] Zhecheva A, Sha W, Malinov S, Long A. Enhancing the microstructure and properties of titanium alloys through nitriding and other surface engineering methods. Surf Coat Technol 2005;200:2192–207. https://doi.org/10.1016/j.surfcoat.2004.07.115.

[20] Bernuy-Lopez C, Bexell U, Stenstrom M, Norrby N, Westlinder J. The time for industrialization has come: a pre-coated solution for the GW scale. ECS Trans 2021;103:1803–8. https://doi.org/10.1149/10301.1803ecst.

[21] Jo A, Ju H. Numerical study on applicability of metal foam as flow distributor in polymer electrolyte fuel cells (PEFCs). Int J Hydrogen Energy 2018;43:14012–26. https://doi.org/10.1016/j.ijhydene.2018.01.003.

[22] Baroutaji A, Carton JG, Stokes J, Olabi AG. Application of open pore cellular foam for air breathing PEM fuel cell. Int J Hydrogen Energy 2017;42:25630–8. https://doi.org/10.1016/j.ijhydene.2017.05.114.

[23] Stiber S, Sata N, Morawietz T, Ansar SA, Jahnke T, Lee JK, Bazylak A, Fallisch A, Gago AS, Friedrich KA. A high-performance, durable and low-cost proton exchange membrane electrolyser with stainless steel components. Energy Environ Sci 2022;15:109—22. https://doi.org/10.1039/d1ee02112e.

[24] Grigoriev SA, Millet P, Volobuev SA, Fateev VN. Optimization of porous current collectors for PEM water electrolysers. Int J Hydrogen Energy 2009;34:4968—73. https://doi.org/10.1016/j.ijhydene.2008.11.056.

[25] Lee B, Lee T, Lee Y, Lee DJ, Jeong J, Yuh J, Oh SH, Kim HS, Lee CS. Space-holder effect on designing pore structure and determining mechanical properties in porous titanium. Mater Des 2014;57:712—8. https://doi.org/10.1016/j.matdes.2013.12.078.

[26] T.U.D. of E. (DOE) E.E. and R.E.. Fuel cell technologies office, fuel cells. In: Multi-year research. Development and Demonstration Plan; 2016. 3.4.1-3.4.58.

[27] Schindelin J, Arganda-Carreras I, Frise E, Kaynig V, Longair M, Pietzsch T, Preibisch S, Rueden C, Saalfeld S, Schmid B, Tinevez J-Y, White DJ, Hartenstein V, Eliceiri K, Tomancak P. A. Cardona, Fiji: an open-source platform for biological-image analysis. Nat Methods 2012;9:676. https://doi.org/10.1038/nmeth.2019. https://www.nature.com/articles/nmeth.2019#supplementary-information.

[28] Münch B, Holzer L. Contradicting geometrical concepts in pore size analysis attained with electron microscopy and mercury intrusion. J Am Ceram Soc 2008;91:4059—67. https://doi.org/10.1111/j.1551-2916.2008.02736.x.

[29] Wang H, Sweikart MA, Turner JA. Stainless steel as bipolar plate material for polymer electrolyte membrane fuel cells. J Power Sources 2003;115:243—51. https://doi.org/10.1016/S0378-7753(03)00023-5.

[30] Chirico C, Tsipas S, Toptan F, Gordo E. Development of Ti—Nb and Ti—Nb—Fe beta alloys from TiH2 powders. Powder Metall 2019;62:44—53. https://doi.org/10.1080/00325899.2018.1563953.

[31] Biesinger MC, Lau LWM, Gerson AR, Smart RSC. Resolving surface chemical states in XPS analysis of first row transition metals, oxides and hydroxides: Sc, Ti, V, Cu and Zn. Appl Surf Sci 2010;257:887—98. https://doi.org/10.1016/j.apsusc.2010.07.086.

[32] Piscanec S, Ciacchi LC, Vesselli E, Comelli G, Sbaizero O, Meriani S, De Vita A. Bioactivity of TiN-coated titanium implants. Acta Mater 2004;52:1237—45. https://doi.org/10.1016/j.actamat.2003.11.020.

[33] Wang Y, Northwood DO. An investigation into TiN-coated 316L stainless steel as a bipolar plate material for PEM fuel cells. J Power Sources 2007;165:293—8. https://doi.org/10.1016/j.jpowsour.2006.12.034.

[34] Pan J, Thierry D, Leygraf C. Electrochemical impedance spectroscopy study of the passive oxide film on titanium for implant application. Electrochim Acta 1996;41:1143—53. https://doi.org/10.1016/0013-4686(95)00465-3.

[35] Orsi A, Kongstein OE, Hamilton PJ, Oedegaard A, Svenum IH, Cooke K. An investigation of the typical corrosion parameters used to test polymer electrolyte fuel cell bipolar plate coatings, with titanium nitride coated stainless steel as a case study. J Power Sources 2015;285:530—7. https://doi.org/10.1016/j.jpowsour.2015.03.111.